

## RESEARCH ARTICLE

# A table-top PXI based low-field spectrometer for solution dynamic nuclear polarization

Joshua R. Biller  | Karl F. Stupic | J. Moreland

Physical Measurement Laboratory,  
National Institute of Standards and  
Technology, Boulder, CO, USA

## Correspondence

Joshua R. Biller, Physical Measurement  
Laboratory, National Institute of  
Standards and Technology, 325 Broadway,  
Boulder, CO 80305, USA.  
Email: joshua.biller@nist.gov

We present the development of a portable dynamic nuclear polarization (DNP) instrument based on the PCI eXtensions for Instrumentation platform. The main purpose of the instrument is for study of  $^1\text{H}$  polarization enhancements in solution through the Overhauser mechanism at low magnetic fields. A DNP probe set was constructed for use at 6.7 mT, using a modified Alderman–Grant resonator at 241 MHz for saturation of the electron transition. The solenoid for detection of the enhanced  $^1\text{H}$  signal at 288 kHz was constructed with Litz wire. The largest observed  $^1\text{H}$  enhancements ( $\epsilon$ ) at 6.7 mT for  $^{14}\text{N}$ -CTPO radical in air saturated aqueous solution was  $\epsilon \sim 65$ . A concentration dependence of the enhancement is observed, with maximum  $\epsilon$  at 5.5 mM. A low resonator efficiency for saturation of the electron paramagnetic resonance transition results in a decrease in  $\epsilon$  for the 10.3 mM sample. At high incident powers (42 W) and long pump times, capacitor heating effects can also decrease the enhancement. The core unit and program described here could be easily adopted for multi-frequency DNP work, depending on available main magnets and selection of the “plug and play” arbitrary waveform generator, digitizer, and radiofrequency synthesizer PCI eXtensions for Instrumentation cards.

## KEYWORDS

$^1\text{H}$ , DNP, Hyperpolarization, LabVIEW, Nitroxide, PXI, Resonator efficiency

## 1 | INTRODUCTION

Dynamic nuclear polarization (DNP) is a technique for enhancing the polarization of nuclear spins in the vicinity of unpaired electrons. The mechanisms which determine the magnitude of enhancement vary. At high magnetic fields and in the solid state, the enhancement is described by considering the number of interacting spins contributing to the enhancement: two spins (solid effect<sup>[1–4]</sup>), three

spins (cross effect<sup>[5,6]</sup>) or multiple spins (thermal effect<sup>[7]</sup>). In solution, the molecule containing the unpaired electron and the proton are tumbling rapidly, and enhancement is determined by the Overhauser effect (OE). The magnitude of the OE is dependent on the time scale modulating the interaction between electron and nuclear spins and the distance of closest approach. The OE is the longest studied DNP mechanism, going back over 60 years to the first experimental demonstrations.<sup>[8,9]</sup>

The general expression for the enhancement ( $\epsilon$ ) is given by Equation 1

$$\epsilon = 1 - \rho_S f \left| \frac{\gamma_S}{\gamma_I} \right| \quad (1)$$

Contribution of the National Institute of Standards and Technology; not subject to copyright in the United States. Certain commercial instruments and software are identified to specify the experimental study adequately. This does not imply endorsement by NIST or that the instruments and software are the best available for the purpose.

where  $\rho$  is the coupling factor,  $s$  is the saturation factor, and  $f$  is the leakage factor. The ratio of the electron gyromagnetic ratio ( $\gamma_s = 28024.951$  MHz/T) to the proton gyromagnetic ratio ( $\gamma_I = 42.576$  MHz/T) results in the maximum possible enhancement,  $\epsilon = +658$  for scalar coupling ( $\rho = s = f = 1$ ) or  $\epsilon = -329$  for dipolar coupling ( $\rho = 0.5, s = f = 1$ ). There is an extensive literature on the theoretical background for general OE-DNP,<sup>[10–12]</sup> which has been recently reviewed.<sup>[13]</sup> Nitroxides are the class of radicals most studied for solution DNP<sup>[11,14–23]</sup> and for these radicals Equation 1 is an oversimplification. The complicating factor is the presence of a  $^{14}\text{N}$  nucleus ( $I = 1$ ) in the nitroxide structure, which splits the electron paramagnetic resonance (EPR) transition into three hyperfine lines. Saturation may be transferred from one line to the other two either by high concentrations (Heisenberg exchange)<sup>[24,25]</sup> or by modulation of the  $^{14}\text{N}$  nuclear relaxation time,  $T_{1\text{N}}$ <sup>[25]</sup> depending on the tumbling correlation time,  $\tau_R$ , of the radical.

### 1.1 | The coupling factor ( $\rho$ )

The coupling factor depends on the cross relaxation between the unpaired electron and the proton. Cross-relaxation can occur either through purely dipolar or scalar mechanisms, or a combination of the two. The value of  $\rho$  for nitroxides in solution at low magnetic field is assumed to be exclusively dipolar,<sup>[12]</sup> although inclusion of only a very small amount (5–10%) of scalar contribution could result in appreciable changes in  $\rho$ .<sup>[13]</sup> For dipolar coupling, a distance of closest approach between the radical center (nitroxide) and proton on the water molecule of about 2.9 Å facilitates the largest enhancements.<sup>[26]</sup> Knowledge of the closest approach and translational correlation time allows for calculations of the diffusion coefficients of the water and radical. If  $\rho$  can be determined with certainty from study of  $\epsilon$ ,  $s$ , and  $f$ , information on the molecular dynamics of the system under study can be extracted.<sup>[19,27–29]</sup>

### 1.2 | The leakage factor, $f$

The leakage factor reflects the enhanced nuclear relaxation in the presence of the paramagnetic nitroxide molecule. As radical concentration increases, the ratio approaches unity. The leakage factor can be calculated by measuring the spin–lattice relaxation time in the absence of radical ( $T_{10}$ ) and at each radical concentration used for the DNP experiment ( $T_1$ ) according to Equation 2.

$$f = 1 - \frac{T_1}{T_{10}} \quad (2)$$

### 1.3 | The saturation factor, $s$

For nitroxide radicals at high concentrations, the  $s$ -factor is heavily influenced by Heisenberg exchange (HE), which transfers polarization between the three lines of a  $^{14}\text{N}$  nitroxide spectrum. A model accounting for HE was initially developed in 1977,<sup>[24]</sup> then reintroduced in combination with the effect of  $T_{1\text{N}}$  (for the  $^{14}\text{N}$  nucleus on the radical structure) in 2007.<sup>[25]</sup> Experimental measurements of  $s$  have been made with pulsed electron nuclear double resonance experiments<sup>[30]</sup> or by observing the paramagnetic shift<sup>[26]</sup> at high magnetic fields. Quantitative values of  $s$  are required for calculation with good precision of  $\rho$ .

### 1.4 | Temperature changes effect the DNP experiment in a variety of ways

Work at both intermediate (0.35 T)<sup>[29]</sup> and high field (7.3 T)<sup>[31]</sup> have studied the sensitivity of  $\epsilon$  to small changes in sample temperature via modulation of  $f$  or  $\rho$ , respectively. At 0.35 T, temperature modulation of  $f$  was most pronounced at radical concentrations  $< 1$  mM.<sup>[29]</sup> If  $B_0$  homogeneity is high enough, the shift in resonance position of water<sup>[32]</sup> or mixtures of water; ethylene glycol<sup>[26]</sup> have been used to assess temperature change during DNP experiments. Temperature changes on the order of 50 °C are observed for small samples at high field, which increases the coupling factor and result in a linear increase in  $\epsilon$  versus  $\Delta T$ .<sup>[31]</sup> Because the coupling factor in the low field regime is at the dipolar limit<sup>[12]</sup>, an increase in temperature is not likely to contribute in the same way for radicals in solution. The shift in resonance position due to temperature is only on the order of a few ppm which is below the homogeneity of low field systems operating below  $\sim 5$  MHz (0.117 T). Changes in sample temperature could also be expected to impact the saturation factor by modulating  $T_{1\text{H}}$ ,  $T_{1\text{e}}$  or enhancing the Heisenberg exchange rate.

### 1.5 | Solution DNP at low magnetic field

Specific treatment has been given to OE-DNP in magnetic fields  $< 10$  mT<sup>[20,33–35]</sup> and in Earth's magnetic field.<sup>[36]</sup> In addition, electron transitions that are forbidden at higher magnetic field strengths are observable, and the spectrum becomes more complicated (e.g., Figure 4 in<sup>[39]</sup>). When the applied static magnetic field in the experiment ( $B_0$ ) begins to approach the magnitude of hyperfine splitting ( $A_{\text{N}}$ ) between the three lines of a  $^{14}\text{N}$  nitroxide, there are additional considerations. The ratio of 658 $\times$  determined by the gyromagnetic constants at high field is based on  $B_0$  as the dominant component of the field seen by the

spins. As  $B_0$  approaches and becomes less than  $A_N$ , the dominant field component seen by the spins becomes  $A_N$ . As applied  $B_0 \ll A_N$  enhancements closer to  $2,000\times$  have been observed with nitroxide radicals<sup>[40]</sup> It has also been proposed that at low magnetic field, the theoretical maximum enhancement should vary for each of three lines of the  $^{14}\text{N}$  nitroxide as  $\omega_S/\omega_I$  rather than  $\gamma_S/\gamma_I$ .<sup>[24]</sup>

## 1.6 | Motivation for work

Many previous OE-DNP studies have taken advantage of either a commercial nuclear magnetic resonance (NMR) console or commercial EPR console as part of the instrument setup. For laboratories without access to such systems, this is a major barrier to implementing DNP experiments. Recently, instruments based on a PCI eXtensions for Instrumentation (PXI) platform have been constructed for NMR<sup>[41,42]</sup> and Mossbauer spectroscopy

experiments.<sup>[43,44]</sup> The PXI architecture offers easy synchronization, modularity and portability. A wide array of “plug-and-play” arbitrary waveform generator (AWG), digitizer cards and radiofrequency (RF) generators are available from over different 55 vendors for easy instrument customization. Here, we describe a table-top low field PXIe based instrument for DNP. Along with the hardware, software to run the experiment and a front-panel were developed using LabVIEW. By constructing the instrument from a set of widely available commercial boards, we lower the barrier for groups who may wish to make use of the Overhauser experiment as part of their research.

Careful consideration of experimental<sup>[26]</sup> and resonator conditions<sup>[31]</sup> at high magnetic fields has shown sizeable DNP enhancements can be achieved, even up to fields of 9 T. These very recent and exciting observations are in direct conflict with the “established” theory for solution OE DNP that predicts loss of enhancement at

**TABLE 1** Information on components used for construction of the low field digital DNP spectrometer. <sup>1</sup>Vendor key: National Instruments (NI), E&I, Ltd. (EI), Mini-Circuits (MC), Tecmag (TM), Omicron Lab (OL), Copper Mountain (CM) Mathworks (MW), Hewlett-Packard (HP), Tekelec-Temex (TT), Voltronics (VT), American technical ceramics (ATC), Formlabs (FL), EtekCity (EC), and Opsens (OS)

Vendor	Model number	Specifications
NI	PXIe-1071	4-slots, 10 and 100 MHz reference clocks
NI	PXIe-8135	2.3 GHz quad-core processor with windows OS
NI	PXI-5412	100 MS/s, 14-bit AWG 10 kHz–20 MHz
NI	PXIe-5122	100 MS/s, 14-bit digitizer
NI	PXI-5650	500 kHz–1.3 GHz RF generator
EI	2200 L	200 W, 10 kHz–12 MHz CW amplifier
MC	LZY-1+	50 W, 20–512 MHz CW amplifier
TM	Special order	Passive T/R switch
NI	2014 SP1	LabVIEW software for controlling instrument
OL	Bode 100 VNA	Portable USB VNA (1 Hz–40 MHz)
CM	Planar TR1300/1	Portable USB VNA (300 kHz–1.3 GHz)
HP	8447F	Low noise preamplifier, 100 kHz–1.3 GHz
HP	8447A	Low noise preamplifier, 100 kHz–400 MHz
MW	R2014b	Matlab software for fitting $T_1$ saturation recovery data
VT	NHMTM130C	Extended range glass trimmer capacitor, 2–130 pF
TT	5500	Variable piston precision trimmer capacitor, 1–20 pF
VT	P5J	Sapphire dielectric trimmer capacitor, 0.6–4.5 pF
ATC	Various	Non-magnetic ceramic static capacitors
FL	Form 2	3D printer
EC	ETC8550	Infrared thermometer
OS	L-014-0105-02	Fiberoptic sensor

CW = continuous wave; VNA = vector network analyzer.

<sup>1</sup>Certain commercial instruments and software are identified to specify the experimental study adequately. This does not imply endorsement by NIST or that the instruments and software are the best available for the purpose.

high magnetic fields, as the electron Larmor frequency becomes much larger than the timescale of the dipolar interaction modulating the polarization transfer. It turns out that fast *local* dynamics can increase the  $\rho$  to the point where sizable enhancements are achievable.<sup>[13]</sup> It is now time to apply the same methods for quantitative solution DNP which have been deployed at high<sup>[45]</sup> and intermediate fields<sup>[25,29]</sup> to the low-field regime, to investigate if the estimates of maximum  $\epsilon$  at low-field were also too conservative. Towards this end, use of inexpensive commercial cards which adhere to strict electrical and mechanical standards could facilitate an easily reproduced standard solution DNP spectrometer which could be constructed at multiple labs for comparison of experimental results.

## 2 | SYSTEM COMPONENTS

### 2.1 | Instrument hardware

The first step in building a digital low-field DNP system was to build a digital low field NMR spectrometer. Full detail of the NMR spectrometer has been previously published.<sup>[42]</sup> Table 1 lists part numbers and vendors for all the hardware which make up the spectrometer.

The heart of the instrument is a portable PXI chassis with an embedded controller, arbitrary waveform card (AWG 14-bit, 100 MS/s) for  $^1\text{H}$  pulse generation, digitizer card (14-bit, 100 MHz/s) for data collection, and RF generator card (20 MHz–1.3 GHz) for output at the EPR frequencies (Figure 1a). The AWG card can operate up to 25 MHz corresponding to 0.6 T for  $^1\text{H}$ . The output from the AWG is routed into a nominally 200 W amplifier with operating range from 10 kHz to 12 MHz. The RF card can operate up to 1.3 GHz, and is routed into a 50 W amplifier operating from 20 to 500 MHz. The experiment is

composed of a polarization period ( $T_{\text{DNP}}$ ) followed by an acquisition period (Figure 1c).

### 2.2 | Instrument software

The instrument interface was programmed using LabVIEW 2014 SP 1, along with extra drivers downloaded for the AWG (NI-FGEN) and digitizer (NI-Scope) and RF signal generator. A passive T/R switch on the NMR side eliminated transistor–transistor logic signaling requirements and simplified the design. The programming flow is provided schematically in Figure 2. The full software

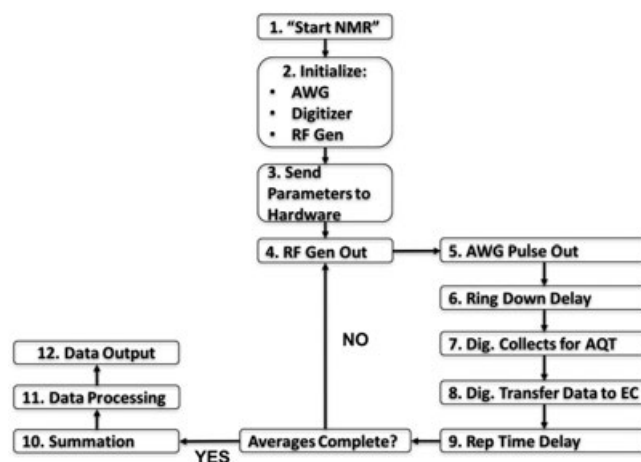


**FIGURE 2** Programming diagram for dynamic nuclear polarization (DNP) software. Although the LabVIEW programming environment was chosen to control the instrument in this report, the same program flow could be reproduced using PyVISA (python) or the Instrument Control Toolbox (Matlab). NMR = nuclear magnetic resonance; AWG = arbitrary waveform generator; RF = radiofrequency; AQT = Acquisition Time; EC = Embedded Controller

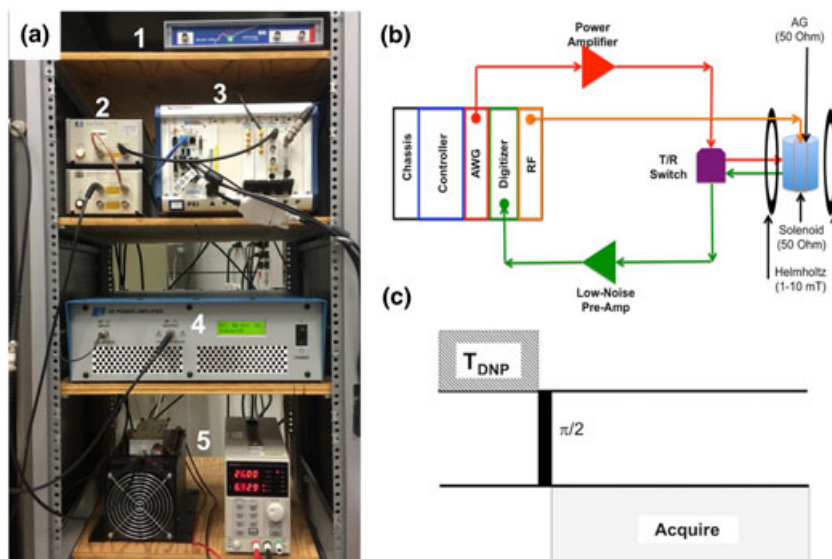


**FIGURE 1** The base PCI extensions unit. (a) Spectrometer components—vector network analyzer for tuning nuclear magnetic resonance coils (1), low-noise preamplifiers (2), PCI extensions spectrometer unit (3), nuclear magnetic resonance amplifier (4), electron paramagnetic resonance amplifier and power supply (5). Not pictured is USB vector network analyzer for electron paramagnetic resonance coil tuning. (b) Instrument schematic including coils and main magnet. (c) Saturation sequence for dynamic nuclear polarization (DNP) experiment. RF = radiofrequency; AWG = arbitrary waveform generator

detail will be published elsewhere. The overall architecture is an event driven state machine with queued message handling (Fig. S2). Thirty-eight cases are responsible for running the NMR side of the experiment, and an additional four cases control the RF output and synchronize execution of the NMR side afterwards. The case structures provide efficient and clean handling of code fragments.

### 2.3 | Calibration of RF amplifier for EPR excitation

The power output of the EPR amplifier measured as a function of input power from  $-8$  to  $+7$  dBm is plotted in Figure 3. The power amplifier is specified to provide  $+42$  dB gain, with maximum input of  $+10$  dBm. From  $-8$  to  $+3$  dBm ( $0.16$ – $2$  mW), amplifier output was between  $42$  and  $43$  dB ( $3.2$ – $33.8$  W). From  $+4$  up to  $+7$  dBm input ( $2.5$ – $5$  mW) amplifier gain dropped off to  $39.3$  dB and the maximum output was  $42.3$  W at  $+7$  dBm input. Past  $+7$  dBm input, the amplified sine-wave became severely distorted. The enhancement for each concentration was measured as function of power over the entire power output range of  $3.2$ – $42.3$  W.

### 2.4 | Resonator design/assembly

Resonant circuits are used to couple the instrument into the spins under study. With a target operating frequency (presented in radians,  $\omega = 2\pi f$ ) and corresponding inductance ( $L_H$ ) and resistance ( $R$ ), the capacitances required to tune ( $C_T$ ), and match ( $C_M$ ) to a  $50 \Omega$  load ( $Z_0 = 50$ ) can be calculated using Equations 3 and 4.

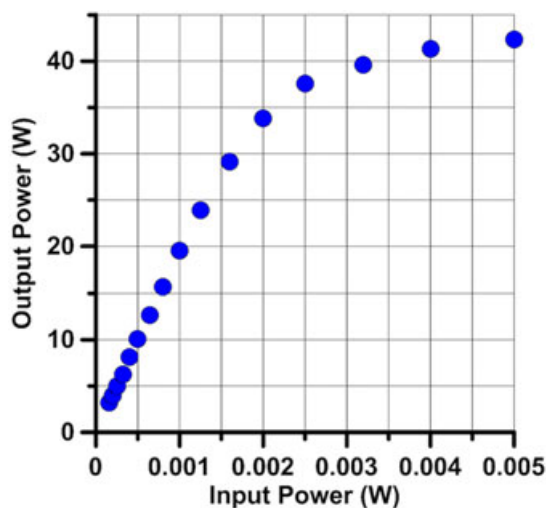


**FIGURE 3** Calibration of the power amplifier used in the dynamic nuclear polarization experiments

$$C_T = \left(\frac{1}{\omega}\right)^2 \frac{1}{L_H} \quad (3)$$

$$C_M = \frac{RC_T}{2Z_0} + \sqrt{\frac{RL_H C_T^2}{Z_0(L_H - RC_T Z_0)} + \left(\frac{RC_T}{2Z_0}\right)^2} \quad (4)$$

For the NMR side resonant circuit (solenoid), copper traces were patterned on one side of a circuit board with space for a variety of capacitors to be placed in parallel ( $C_T$ ) or series ( $C_M$ ). A close up of the printed circuit board is shown in Figure 4c, and an example of a tuned circuit is shown in Figure 4b. Each printed circuit board was placed inside a shielded aluminum box with BNC attached connectors. Two portable USB VNA (vector network analyzer) instruments (Table 1) were used to assess tune frequency and matching. VNA-1 covered frequencies between  $1$  Hz and  $40$  MHz, and included an impedance adapter that could be used to measure  $L_H$  and  $R$ . The resonator  $Q$  was calculated using the  $-3$  dB bandwidth and center frequency. VNA-2 covers frequencies between  $300$  kHz and  $1.3$  GHz, and was used for construction and tuning of the EPR resonators.

### 2.5 | NMR probe for measurement of $T_{1H}$

An NMR solenoid was constructed of  $N = 49$  turns of  $405/44$  Litz wire on a coil form ( $6$  cm I.D.  $\times$   $8.25$  cm long). The solenoid was used to make measurements of  $T_{1H}$  in water or with dissolved radical to calculate the leakage factor. The operating frequency for these measurements was  $456$  kHz ( $10.7$  mT), for which the measured inductance was  $L_H = 81 \mu\text{H}$ , with a measured resistance  $R = 922$  m $\Omega$ . The matching capacitance was a single trimmer capacitor with range from  $2$  to  $130$  pF (Table 1). The tuning capacitance was a static  $1.34$  nF, in addition to another  $2$ – $130$  pF trimmer capacitor. The measured  $Q$  of the loaded resonator was  $200$ .

### 2.6 | DNP probe set—( $6.7$ mT) $241$ MHz (EPR), $288$ kHz (NMR)

The DNP probe set is shown in Figure 4a. A modified Alderman–Grant (MAG) resonator following the design of<sup>[46]</sup> was used for the EPR probe at  $6.7$  mT. Both the original AG,<sup>[37]</sup> and the recent modification<sup>[46]</sup> were designed to reduce electric-field and therefore sample heating. AG resonators have also recently been deployed for DNP at S-band frequencies ( $73$  mT)<sup>[47]</sup> for DNP and at  $250$  MHz<sup>[48]</sup> for EPR imaging. A probe form for the MAG was 3D printed (Table 1) using Clear<sup>®</sup> resin. The former dimensions were  $2.7$  cm I.D.  $\times$   $5.6$  cm long, and

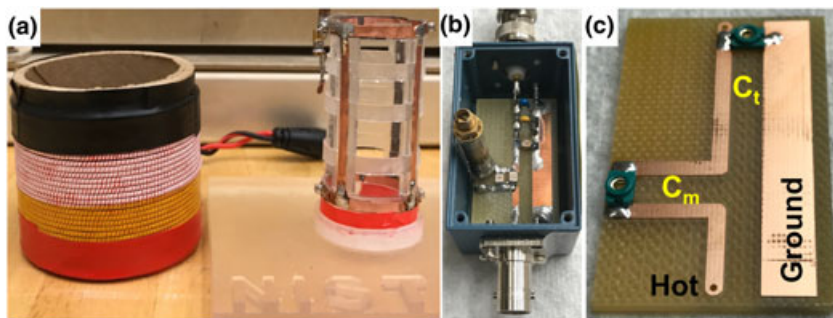


**FIGURE 4** (a) Resonator assemblies used for dynamic nuclear polarization experiments. A modified Alderman–Grant resonator housed inside the nuclear magnetic resonance solenoid for experiments at 6.7 mT. (b) The tune box used for the nuclear magnetic resonance solenoid. (c) Close up of the printed circuit board with copper traces and labels for placement of capacitor in series ( $C_m$ ) or in parallel ( $C_t$ ). For detailed description of the Alderman–Grant design, the reader is directed to Figures 1 and 2 in ref. [37]. Three different methods for connecting the Alderman–Grant resonator are given in ref. [38] (2nd edition, page 515, Figure 8.33)

copper adhesive tape (3.18 mm wide  $\times$  0.5 mm thick) was used for the legs and inner and outer guard rings.

The separation between inner and outer guard rings was 2 mm. The Clear<sup>®</sup> resin is a mixture of methacrylic esters, the exact nature and formulation of which is proprietary. Dielectric values for methacrylate polymer were found in the literature ( $\epsilon \sim 4$ )<sup>[49]</sup> and used in the calculation of the capacitance between inner and outer guard rings. Four 15 pF static capacitors (Table 2) were placed across the gaps between the “legs” (or H-sections) of the resonator and the outer end rings. The value of  $C_T$  is reflected in the capacitance across the legs and end rings, in addition to the capacitance between the inner and outer guard rings. Calculation of the capacitance across the gap = 4.1 pF, the value of  $C_T$  is approximately = 15 pF + 4.1 pF/4 = 16 pF. From this value, the inductance of the MAG coil was calculated as  $L_H = 27$  nH. The loaded  $Q = 86$  was measured with VNA-2. An estimate of the MAG efficiency was made by calculating the  $B_1$  field that would be produced based on the dimensions of the resonator and using equations provided in.<sup>[38]</sup> The calculated efficiency for the MAG in the 6.7 mT probeset is  $23 \mu\text{T}/\sqrt{W}$ .

The probe set corresponded to the  $T_{16}$  transition of the nitroxide radical ( $m_I = +1$  at high field). The solenoid for NMR detection was placed outside the MAG, and constructed with 405/44 Litz wire (6 cm I.D.  $\times$  5 cm), as the  $Q$  values of Litz wire resonators are usually higher than

those made from solid copper wire at low frequency.<sup>[50,51]</sup>

The measured inductance was  $L_H = 40 \mu\text{H}$ , and resistance = 0.722  $\Omega$ . For 288 kHz, this required values of  $C_T = 7.6$  nF and  $C_M = 1$  nF.

## 3 | EXPERIMENT DETAIL

### 3.1 | Samples

The free radical 2,2,5,5-tetramethyl-1-pyrrolidinyloxy (<sup>14</sup>N CTPO, Sigma Aldrich) was dissolved directly into 30 ml of de-ionized (D.I.) water for a final concentration of 10.3 mM. Dilutions of this stock were made for final concentrations of 5.5, 2.2, 1 and 0.67 mM. Approximately 15 ml of solution was inserted into glass vials (21 mm o. d.  $\times$  71 mm high, Kimble Chase) which were then placed into the center of the DNP resonator assembly for analysis.

### 3.2 | Collection of DNP enhancements

For each test, the main magnet was allowed to warm up for at least half an hour. Temperature at the resonator was monitored with an infrared heat gun (Table 1) and varied between 24 and 25  $^{\circ}\text{C}$  for all measurements. An attempt was made to mitigate transient heating effects by providing ample time between RF irradiations. For the concentration series, each measurement was done in

**TABLE 2** Calculation of the leakage factor for radical solutions from 0.67 to 10.3 mM. The upper limit of the leakage factor is  $f = 1$

	Water	0.67 mM	1 mM	2.2 mM	5.5 mM	10.3 mM
$T_{1H}(s)$	2.5	0.95	0.84	0.57	0.24	0.14
Conf. (95%)	2.26–2.76	0.87–1.04	0.70–0.91	0.54–0.61	0.21–0.27	0.12–0.15
$f$		0.62	0.66	0.77	0.90	0.94
Conf. (95%)		0.54–0.70	0.57–0.77	0.68–0.86	0.76–1.04	0.8–1.08

triplicate, with at least one of the three measurements done on a different day, and/or at different times in the same day. Reproducibility between replicates was good (Figure S3). To calculate the enhancement, the amplitude of spectra collected with EPR “on” was divided by the spectral amplitude with EPR “off”. An example of the  $^1\text{H}$  spectrum in the presence or absence of DNP enhancement is shown in Figure S1.

For each DNP experiment, and for pump time experiments, the center frequency was recorded before and after the experiment by measurement on VNA-2. The maximum observed change in the center frequency was  $\sim 0.3$  MHz, indicating no permanent shift in resonator characteristics as a result of the incident power. Transient shifts in resonator frequency and tuning could be caused by rapid heating during the highest incident powers.

## 4 | RESULTS

### 4.1 | Measurement of $T_{1\text{H}}$ by single pulse saturation recovery.

$T_{1\text{H}}$  was measured for D.I. water and each radical concentration with single-pulse-saturation-recovery (SPSR)<sup>[42]</sup> for calculation of the leakage factor,  $f$ . Triplicate measurements were acquired at each repetition time, and data points were fit using the data processing software in Table 1. Figure 5a shows an example recovery spectrum for the 2.2 mM  $^{14}\text{N}$  CTPO sample, with a measured  $T_{1\text{H}} = 0.57 \pm 0.04$  s. Figure 5b shows  $1/T_{1\text{H}}$  versus concentration for the whole series. The temperature change over the course of the experiment was 24–25 °C, as measured by the Inversion Recovery (IR) gun.

There is a good linear fit ( $R^2 = 0.997$ ) in the change of  $T_{1\text{H}}$  versus nitroxide radical concentration. If there was substantial temperature variation between measurements of  $T_{1\text{H}}$  for different radical concentrations, the linear fit would be poor. This supports the acquisition of  $T_{1\text{H}}$  SPSR and stability in the sample temperature while the measurements were being carried out. However, the error in the measurement of  $T_1$  is approximately 8–10%, as judged by the 95% confidence interval calculated for each fit.

Propagation of the error through the calculation of  $f$  using Equation 2 results in a wide confidence interval for  $f$  (Table 2). Because calculation of  $\rho$  at intermediate fields is dependent on  $\epsilon$ ,  $s$ , and  $f$ , the error for each of these quantities should be minimized so that a value of  $\rho$  with a narrow confidence interval can be obtained. The SPSR does not make use of phase cycling, although tip angle optimizations are performed for each  $\pi/2$  pulse. We are currently evaluating other models of AWG card with the ability to program in composite pulses with an 8-step phase cycle for a traditional inversion recovery experiment, with the aim of reducing the error in measurement of  $T_{1\text{H}}$  and therefore in calculation of the leakage factor.

### 4.2 | Selection of DNP pump time

Because values of  $T_{\text{DNP}}$  need to be sufficiently long relative to  $T_{1\text{H}}$ , enhancement versus  $T_{\text{DNP}}$  plots were gathered for each concentration (Figure 6) at the highest incident power to ensure fullest achievable saturation. Pump time experiments were collected at maximum power from RF amplifier, 42.3 W for the  $^{14}\text{N}$  CTPO concentration series. From these plots, a pump time was selected that gave the maximum  $\epsilon$ , and this time was used when collecting enhancement vs. incident power data.

At longer pump times, the enhancement decreases. The effect is more apparent at higher incident powers (Figure 6c). Temperature measured with the infrared thermometer only showed variation of about 1 °C over the course of the experiment when measuring in the immediate vicinity of the sample. To further investigate temperature change at the sample, a fiberoptic sensor (Table 1) was inserted into the 10.3 mM sample through a small hole in the top of the tube and the pump time series was repeated. For application of continuous wave power for 12 s, the change in temperature of the solution assessed by the fiberoptic sensor was 0.2, 0.8, and 1.2 °C for incident powers of 5, 20, and 40 W, respectively. Increase in  $T_{1\text{H}}$  due to temperature has resulted in increases in  $\epsilon$ ,<sup>[29]</sup> which is opposite of the observation in Figure 6. In addition, the change in temperature of 1.2 °C should not produce a large change in  $T_{1\text{H}}$ .<sup>[45]</sup>

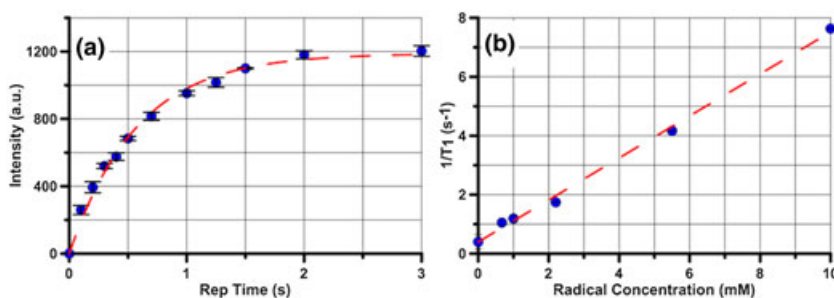


**FIGURE 5** Measurement of  $T_{1\text{H}}$  as a function of radical concentration. (a) Representative single-pulse-saturation-recovery curve for 2.2 mM  $^{14}\text{N}$  CTPO. (b) Linear fit to a plot of  $1/T_{1\text{H}}$  versus concentration from 0 (DI water) to 10.3 mM  $^{14}\text{N}$  CTPO

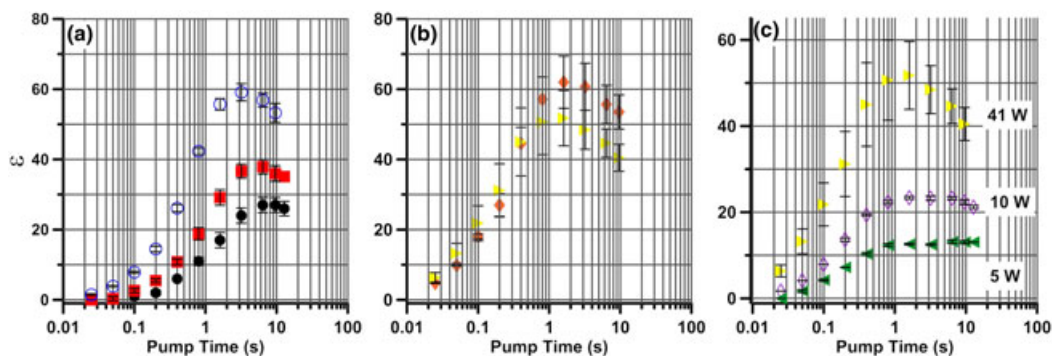


**FIGURE 6** Pump time and enhancement (a) 0.67 mM ( $\bullet$ ), 1.1 mM ( $\blacksquare$ ), 2.2 mM ( $\circ$ ), (b) 5.5 mM ( $\blacklozenge$ ) and 10.3 mM ( $\blacktriangleright$ ). (c) The decrease in enhancement at longer pump times is a function of applied radiofrequency power, as demonstrated with the 10.3 mM solution for powers of 41 W ( $\blacktriangleright$ ), 10 W ( $\blacklozenge$ ), and 5 W ( $\blacktriangleleft$ )

### 4.3 | Concentration series at 6.7 mT

After determination of the correct pump time, enhancement as a function of incident power on the MAG resonator was recorded (Fig. S3). Plots of  $1/\epsilon$  versus  $1/P$  are shown for each concentration in Figure 7. The y-intercept corresponds to the  $\epsilon_{\text{Max}}$  at infinite power. Plots of the  $\epsilon_{\text{obs}}$  for each concentration and calculated  $\epsilon_{\text{Max}}$  are shown in Figure 8. The highest  $\epsilon_{\text{obs}} = 65$  is measured with the 5.5 mM CTPO. Plotting the calculated  $\epsilon_{\text{Max}}$  versus concentration (Figure 8b) and extrapolating to infinite concentration indicates a maximum achievable enhancement  $\epsilon \sim 110$ , which is in agreement with current theory on the maximum enhancement for a single line of a nitroxide in the low magnetic field regime.<sup>[22]</sup>

## 5 | DISCUSSION

The cost of the system described here is about \$ 50k, which is substantially less than the cost of the combination of commercial NMR and EPR spectrometers necessary to run the Overhauser DNP experiment.<sup>[19,52]</sup> No strictly commercial system exists for solution DNP over a wide field/frequency range. Specially designed

commercial systems are available for Earth's field Overhauser Dynamic Nuclear Polarization (ODNP).<sup>[40]</sup> Previously constructed homebuilt low-field DNP spectrometers required extensive engineering skill for fabrication of most of the instrument components.<sup>[53–55]</sup> The PXI Systems Alliance (PXISA) maintains the PXI architecture standard with strict specifications for card performance and interoperability between different vendors. Use of PXI modules, along with off-the-shelf amplifiers, facilitates construction of a “standard” DNP instrument for direct quantitative comparison of DNP enhancements between multiple laboratories.

### 5.1 | Concentration dependence of observed enhancements

Fitting the  $\epsilon_{\text{Max}}$  versus concentration has been previously used to extrapolate the coupling factor at 40 mT.<sup>[56]</sup> The assumptions to support this are as follows: (a) that  $S_{\text{max}} \propto 1$  as concentration increases and (b) Heisenberg spin exchange effects (HE) always increase measured DNP enhancements. Although HE does transfer saturating power, it also increases the electron relaxation rates. If the  $B_1$  delivered is insufficient for those relaxation rates, saturation would decrease with concentration.

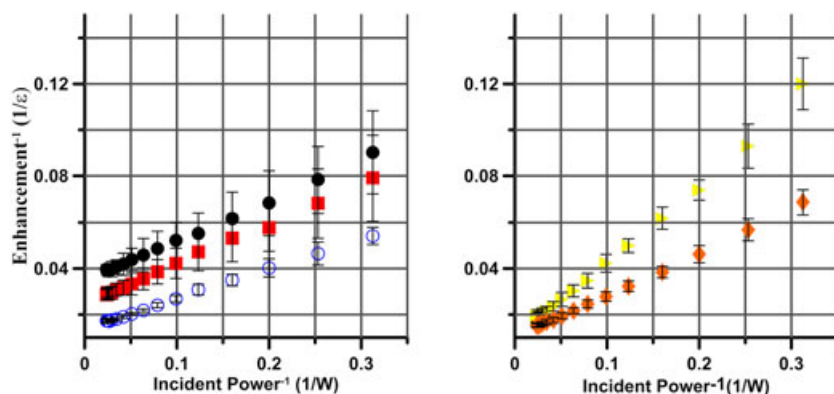


**FIGURE 7** Observed enhancement as a function of radical concentration. The y-intercept of  $1/\epsilon_{\text{Obs}}$  versus  $1/P$  indicates  $\epsilon_{\text{Max}}$  for a given concentration. Concentrations are 0.67 mM ( $\bullet$ ), 1.1 mM ( $\blacksquare$ ), 2.2 mM ( $\circ$ ), 5.5 mM ( $\blacklozenge$ ), and 10.3 mM ( $\blacktriangleright$ )

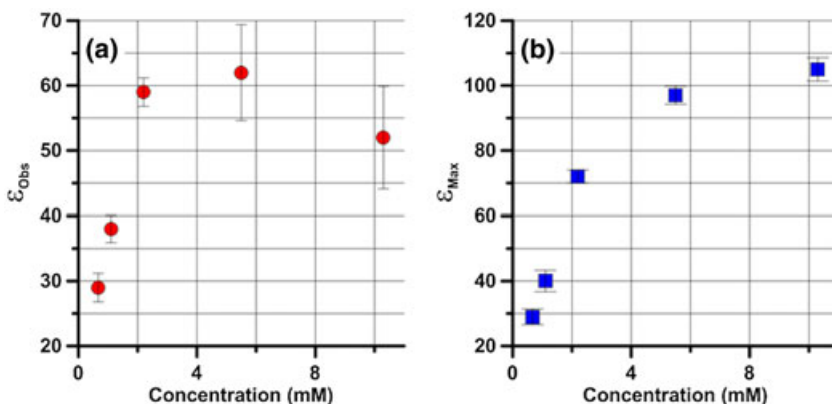


**FIGURE 8** Measured  $\epsilon_{\text{Obs}}$  (a) for each concentration and extrapolated  $\epsilon_{\text{Max}}$  (b) for  $^{14}\text{N}$  CTPO at 6.7 mT.

Van Bentum and co-workers observe an optimum concentration for enhancement between 5 and 15 mM for low  $B_1$  fields.<sup>[45]</sup> Early work in solution DNP at 1.5<sup>[54]</sup> and 10 mT<sup>[23]</sup> also observed a concentration dependence of the enhancement. The saddle coil geometry is common in low-field DNP spectroscopy experiments or low-field Overhauser enhanced magnetic resonance imaging experiments, with very low resonator efficiencies on the order of  $5 \mu\text{T}/\sqrt{\text{W}}$ , and corresponding maximum enhancements at approximately 2 mM<sup>[57,58]</sup>. The resonator efficiency of the MAG resonator used in this work was estimated to be  $23 \mu\text{T}/\sqrt{\text{W}}$ , and the optimum  $\epsilon_{\text{Obs}}$  corresponded to 5.5 mM. Work is currently under way to construct very high efficiency resonators to ensure full saturation at high concentration, and reduce the power requirements for the DNP pumping.

## 5.2 | Decay in enhancement at long DNP pump times

In an attempt to further study transient heating, a 30 dB directional coupler was inserted into the MAG transmit line, and the forward and reverse voltages were monitored on an external oscilloscope. With a pump time = 5 s, the forward/reflected power ratio was 4:1 at 5 W and decreased to ~2:1 at 40 W incident power. When the pump time sequence from 0.25 to 12.8 s was run at 40 W incident power, the forward/reflected ratio was 3.5:1 at 0.25 s and decreased to 1.9:1 at 12.8 s pump time. The increase in reflected power at high incident powers and long DNP pump times indicate substantial change in the resonator tuning and/or match that would result in less power available to saturate the EPR transition, and could explain the decrease in enhancement in the pump time experiments. The similarity in the before/after VNA measurements indicate the temperature induced changes are not permanent. Transient heating of the fixed ceramic capacitors and/or the air-gap trimmer capacitors during the DNP experiment could cause a change in

capacitance and shift either or both the frequency and match.

## 5.3 | Operational limits of system

The RF card, amplifiers and available magnet are the limiting factor on this system. The amplifiers were selected for their lower ends of frequency operation, as the initial instrument motivation is low field DNP, and the current air-core electromagnet is not used above 11 mT. The EPR amplifier was initially selected for its low cost (~\$ 2k), but suffers from non-linearity for output powers >35 W, despite being rated to 50 W. The particular RF generator selected for this unit is only capable of continuous wave operation. It has been shown that pulse-train excitation of the EPR transition can reduce resonator heating, at the expense of saturation.<sup>[55]</sup> More expensive PXIe RF generators are available from multiple vendors that reach up to 20 GHz (~700 mT), which would then allow use of the full range of the AWG up to 20 MHz (~470 mT for  $^1\text{H}$ ) for DNP experiments. A DNP spectrometer with such a range would be powerfully suited for molecular dynamics studies based on measuring  $\rho$  from the change in  $\epsilon$  versus field.

The low-field line ( $m_1 = +1$ ,  $T_{16}$  transition) was chosen for this work because it has given the highest observed enhancement at low-magnetic fields to date.<sup>[17]</sup> Simultaneous pumping of all three hyperfine lines with frequency modulation has been successfully applied at higher magnetic fields.<sup>[59]</sup> Problems arise when considering a frequency modulation or chirp experiment for excitation at low-magnetic field. Consider a general isotropic hyperfine of 16 G for CTPO in water at room temperature. The total width of the spectrum is 32 G, which corresponds to approximately 90 MHz. At an excitation frequency of 241 MHz, a required bandwidth of 90 MHz would require a resonator Q-factor = 2.7. A system designed to be broadband (high impedance) on the EPR transmission side may offer more flexibility for EPR excitation techniques.

Whether or not the higher power requirements of a broadband excitation system would be offset with novel full spectrum excitation techniques would have to be investigated. Due to the wide bandwidth of a typical nitroxide spectrum, this is a limitation of any system constructed at low-field where all components are matched to 50  $\Omega$ .

## 6 | SUMMARY

A DNP system composed of commercially available hardware and software has been presented, with special attention given to the characteristics of the resonator and EPR amplifier which impact the observed enhancement. The operating range of the spectrometer is only limited by the magnet and amplifiers, and the hardware supports expansion of the DNP experiment to 40 mT, or 0.3 T if the RF card is upgraded. Quantitative solution DNP at low magnetic field will be driven by development of more efficient resonators which require less power for saturation of the EPR transition, and thus lower the risk for heating related shifts in resonant frequency or tuning, or sample temperature during the DNP irradiation period.

## ACKNOWLEDGEMENTS

The authors are grateful for discussion of theory and experiment detail of low field DNP with Ryan Barnes and Songi Han (UC-Santa Barbara). David Waddington (University of Sydney) and Matthew Rosen (Harvard/Massachusetts General Hospital) provided guidance on design of the Modified-Alderman Grant resonators used. Thanks also to George Rinard (University of Denver) for discussion of general resonator design.

## ORCID

Joshua R. Biller  <http://orcid.org/0000-0002-3690-0313>

## REFERENCES

- [1] A. Abragam, M. Goldman, *Rep. Prog. Phys.* **1978**, *41*, 395.
- [2] C. Jeffries, *Phys. Rev.* **1957**, *106*, 164.
- [3] A. Abragam, W. G. Proctor, *Hebd. Seance. Acad. Sci.* **1958**, *246*, 2253.
- [4] E. Erb, J. L. Motchane, J. Uebersfeld, *Hebd. Seance. Acad. Sci.* **1958**, *246*, 2121.
- [5] C. F. Hwang, D. A. Hill, *Phys. Rev. Lett.* **1967**, *19*, 1011.
- [6] C. T. Farrar, D. A. Hall, G. J. Gerfen, J. J. Inati, R. G. Griffin, *J. Chem. Phys.* **2001**, *114*, 4922.
- [7] R. A. Wind, M. J. Duijvestijn, C. van der Lugt, A. Manenschijn, J. Vriend, *J. Prog. Nucl. Magn. Reson. Spectrosc.* **1985**, *17*.
- [8] T. R. Carver, C. P. Clichter, *Phys. Rev.* **1953**, *92*, 212.
- [9] T. R. Carver, C. P. Clichter, *Phys. Rev.* **1956**, *102*(4), 975.
- [10] I. Solomon, *Phys. Rev.* **1955**, *99*(2), 559.
- [11] D. Grucker, T. Guiberteau, B. Eclancher, J. Chambron, R. Chiarelli, A. Rassat, G. Subra, B. Gallez, *J. Magn. Reson.* **1995**, *106*, 101.
- [12] W. Muller-Warmouth, K. Meise-Gresch, *Adv. Magn. Reson.* **1983**, *11*, 1.
- [13] E. Ravera, C. Luchinat, G. Parigi, *J. Magn. Reson.* **2016**, *264*, 78.
- [14] S. E. Kucuk, T. Biktagirov, D. Sezer, *Phys. Chem. Chem. Phys.* **2015**, *17*(38), 24874.
- [15] M. Sarracanie, B. D. Armstrong, J. Stockmann, M. S. Rosen, *Magn. Reson. Med.* **2014**, *71*, 735.
- [16] D. Sezer, *Phys. Chem. Chem. Phys.* **2014**, *16*(3), 1022.
- [17] M. D. Lingwood, I. A. Ivanov, A. R. Cote, S. Han, *J. Magn. Reson.* **2010**, *204*(1), 56.
- [18] S. Garcia, J. H. Walton, B. Armstrong, S. Han, M. J. McCarthy, *J. Magn. Reson.* **2010**, *203*, 138.
- [19] B. D. Armstrong, M. D. Lingwood, E. R. McCarney, E. R. Brown, P. Blumler, S. Han, *J. Magn. Reson.* **2008**, *191*(2), 273.
- [20] T. Guiberteau, D. Grucker, *Phys. Med. Biol.* **1998**, *43*(7), 1887.
- [21] T. Guiberteau, D. Grucker, *J. Magn. Reson. A* **1993**, *105*, 98.
- [22] T. Guiberteau, D. Grucker, *J. Magn. Reson. B* **1996**, *110*, 47.
- [23] I. Nicholson, D. J. Lurie, F. J. L. Robb, *J. Magn. Reson.* **1994**, *104*, 250.
- [24] R. D. Bates, W. S. Drozdowski, *J. Chem. Phys.* **1977**, *67*, 4038.
- [25] B. D. Armstrong, S. Han, *J. Chem. Phys.* **2007**, *127*(10), 104508.
- [26] P. Neugebauer, J. G. Krummenacker, V. P. Denysenkov, G. Parigi, C. Luchinat, T. F. Prisner, *Phys. Chem. Chem. Phys.* **2013**, *15*, 6049.
- [27] B. Armstrong, S. Han, *J. Am. Chem. Soc.* **2009**, *131*, 4641.
- [28] J. H. Ortony, C. Cheng, J. M. Franck, R. Kausik, A. Pavlova, J. Hunt, S. Han, *New J. Phys.* **2011**, *13*, 015006.
- [29] J. M. Franck, Pavlova, A., Scott, J.A., Han, S., *Prog. Nucl. Magn. Reson. Spectrosc.*, vol. 0, pp. 33, **2013**.
- [30] M. T. Turke, M. Bennati, *Phys. Chem. Chem. Phys.* **2011**, *13*, 3630.
- [31] M. Gafurov, V. Denysenkov, M. J. Prandolini, T. F. Prisner, *Appl. Magn. Reson.* **2012**, *43*, 119.
- [32] E. V. Kryukov, K. J. Pike, T. K. Tam, M. E. Newton, M. E. Smith, R. Dupree, *Phys. Chem. Chem. Phys.* **2011**, *13*(10), 4372.
- [33] D. J. Lurie, J. S. McLay, I. Nicholson, J. R. Mallard, *J. Magn. Reson.* **1991**, *95*, 405.
- [34] D. J. Lurie, I. Nicholson, J. S. McLay, J. R. Mallard, *Appl. Magnet. Resonance* **1992**, *3*(5), 917.
- [35] D. Grucker, T. Guiberteau, G. Planinsic, *Res. Chem. Intermed.* **1996**, *22*(6), 567.
- [36] K. Lang, M. Moussavi, E. Belorizky, *J. Phys. Chem. A* **1997**, *101*(9), 1662.
- [37] D. W. Alderman, D. M. Grant, *J. Magn. Reson.* **1979**, *36*(3), 447.

- [38] J. Mispelter, M. Lupu, A. Briguet, *NMR Probeheads For Biophysical And Biomedical Experiments*, Imperial College Press, London **2015**.
- [39] M. D. Lingwood, S. I. Han, *Ann. Rep. Nmr Spectrosc.* **2011**, 73, 83.
- [40] M. E. Halse and P. T. Callaghan, *J. Magn. Reson.*, Research Support, Non-U.S. Gov't vol. 195, no. 2, pp. 162, **2008**.
- [41] A. Asfour, "Low-Field NMR/MRI Systems Using LabVIEW and Advanced Data-Acquisition Techniques," in *Practical Applications and Solutions Using LabVIEW Software*, S. Folea, Ed.: InTech, 2011, pp. 17–40.
- [42] J. R. Biller, K. F. Stupic, A. B. Kos, T. Weilert, G. A. Rinard, Y. Nakashima, J. Moreland, *Conc. Magn. Reson B* **2017**.
- [43] J. Pechousek, Prochazka, R., Jancik, D., Frydrych, J., Mashlan, M., "Universal LabVIEW-powered Mossbauer spectrometer based on USB, PCI or PXI devices," presented at the International Conference on the Applications of the Mossbauer Effect **2009**.
- [44] J. Pechousek, "Application of Virtual Instrumentation in Nuclear Physics Experiments," in *Practical Applications and Solutions Using LabVIEW Software*, S. Folea, Ed.: InTech, **2011**, pp. 57–80.
- [45] P. J. M. Van Bentum, G. H. A. van der Heijden, J. A. Villanueva-Garibay, A. P. M. Kentgens, *Phys. Chem. Chem. Phys.* **2011**, 13, 17831.
- [46] D. E. J. Waddington, Sarracanie, M., Salameh, N., Rosen, M., "High performance probe for in vivo Overhauser MRI," presented at the ISMRM 23rd Annual Meeting, **2015**.
- [47] O. Neudert, H. P. Raich, C. Mattea, S. Stapf, K. Munnemann, *J. Magn. Reson.* **2014**, 242, 79.
- [48] S. V. Sundramoorthy, B. Epel, H. J. Halpern, *J. Magn. Reson.* **2014**, 240, 45.
- [49] P. THomas, Ernest Ravindran, R.S., Varma, K.B.R., "Dielectric properties of poly(methyl methacrylate) (PMMA)/CaCuTi4O12 composites," presented at the **2012** IEEE 10th International Conference on the Properties and Applications of Dielectric Materials Bangalore, India, **2012**.
- [50] B. Saam, M. S. Conradi, *J. Magn. Reson.* **1998**, 34(1), 67.
- [51] A. Asfour, Hyacinthe, J.N., Leviel, J.L., "Development of a fully digital and low-frequency NMR system for polarization measurement of hyperpolarized gases," in *IMTC 2006 IEEE Instrumentation and Measurement Technology*, Sorrento, Italy, **2006**, pp. 1839–1843.
- [52] K. Münnemann, C. Bauer, J. Schmiedeskamp, H. W. Spiess, W. G. Schreiber, D. Hinderberger, *Appl. Magnet. Resonance* **2008**, 34(3–4), 321.
- [53] N. Zeghib, D. Grucker, *Phys. Med. Biol.* **2001**, 46(9), 2371.
- [54] I. Sert, M. M. Sunnetcioglu, R. Sungur, G. Bingol, *Z. Naturforsch* **2000**, 55a, 682.
- [55] M. Alecci, D. J. Lurie, *J. Magn. Reson.* **1999**, 138(2), 313.
- [56] S. Garcia, J. H. Walton, B. Armstrong, S. Han, M. J. McCarthy, *J. Magn. Reson.* **2010**, 203(1), 138.
- [57] M. C. Krishna, S. English, K. Yamada, J. Yoo, R. Murugesan, N. Devasahayam, J. A. Cook, K. Golman, J. H. Ardenkjaer-Larsen, S. Subramanian, J. B. Mitchell, *Proc. Natl. Acad. Sci. U.S.A.* **2002**, 99(4), 2216–2221.
- [58] D. D. Jebaraj, H. Utsumi, A. M. F. Benial, *Magn. Reson. Chem.* **2017**.
- [59] Y. Hovav, A. Feintuch, S. Vega, D. Goldfarb, *J. Magn. Reson.* **2014**, 238, 94.

## SUPPORTING INFORMATION

Additional Supporting Information may be found online in the supporting information tab for this article.

**How to cite this article:** Biller JR, Stupic KF, Moreland J. A table-top PXI based low-field spectrometer for solution dynamic nuclear polarization. *Magn Reson Chem.* 2017;1–11. <https://doi.org/10.1002/mrc.4672>